Nano Energy 66 (2019) 104177

Contents lists available at ScienceDirect

Nano Energy

journal homepage: http://www.elsevier.com/locate/nanoen

Full paper

Boosting the sodium storage behaviors of carbon materials in ether-based electrolyte through the artificial manipulation of microstructure

Wei Xiao [a,b,d], Qian Sun [a], Jian Liu [a,c], Biwei Xiao [a], Yulong Liu [a], Per-Anders Glans [c], Jun Li [b], Ruying Li [a], Xifei Li [d,e], Jinghua Guo [c], Wanli Yang [c], Tsun-Kong Sham [b,**], Xueliang Sun [a,*]

[a] Department of Mechanical & Materials Engineering, University of Western Ontario, London, Ontario, N6A 5B9, Canada
[b] Department of Chemistry, University of Western Ontario, London, Ontario, N6A 5B7, Canada
[c] Advanced Light Source, Lawrence Berkeley National Laboratory, Berkeley, CA, 94720, United States
[d] Institute of Advanced Electrochemical Energy, School of Materials Science and Engineering, Xi'an University of Technology, Xi'an, Shaanxi, 710048, China
[e] State Center for International Cooperation on Designer Low-carbon & Environmental Materials (CDLCEM), Zhengzhou University, Zhengzhou, Henan, 450001, China

ARTICLE INFO

Keywords:
Sodium-ion batteries
Carbon anode
Microstructure
Ether-based electrolyte
Co-intercalation
Pseudocapacitive behavior

ABSTRACT

The porous carbon blacks rationally designed by a facile yet efficient NH_3 thermal etching route have been investigated as anode materials in an ether-based electrolyte for sodium-ion batteries. The as-synthesized CBN35 carbon black with a 35% weight loss after NH_3 thermal etching exhibited a large specific charge capacity of 352 mAh g^{-1} at 50 mA g^{-1} and a superior rate capability of 101 mAh g^{-1} at 16000 mA g^{-1}, due to its highest microporosity, an appropriate surface area, a desirable microstructure, and a promising hybrid intercalation mechanism. Impressively, even cycled at 1600 mA g^{-1} over 3200 cycles, an outstanding reversible capacity of 103 mAh g^{-1} with a negligible 0.0162% capacity loss per cycle can still be achieved. Based on the multimodal characterizations including the structural probes of phase evolution for carbon materials, the electrochemical techniques, and the surface-sensitive XAS measurements, the exceptional electrochemical properties should stem from several merits of modified carbon black system. While the particular microporous structure provides relatively more accessible sodium storage sites, a novel hybrid intercalation mechanism in ether-based electrolyte would incorporate the sodium ion insertion into the disordered structure with the solvated sodium ion species co-intercalation into the graphitic phase. In addition to the diffusion-controlled redox reactions, the noticeable surface-induced pseudocapacitive reactions also significantly contribute to the charge storage upon sodiation and guarantee the rapid migrations of sodium ions/solvated compounds. This system further features a controlled emergence of a robust but thin solid electrolyte interphase layer, which could suppress the side reactions of active electrode with reactive electrolyte, maintain the fragile porous structure upon cycling, and facilitate the migrations of sodium ions and solvated sodium ion compounds.

1. Introduction

The commercialization of lithium-ion batteries (LIBs) has stimulated the development of portable electronics and recently envisioned their feasibility for powering electric vehicles [1–3]. However, the huge potential demand for the geologically limited lithium resource along with its soaring prices in recent decades, has propelled the pursuit of sustainable energy storage systems with a low cost and a high reliability [4–6]. Sodium-ion batteries (SIBs), owing to an abundant element reserve with a widespread natural distribution and an appropriate redox potential ($E^{+}_{Na/Na} = -2.71$ V vs. S. H. E) as well as the analogous reaction mechanisms to lithium counterparts, have been extensively studied as promising alternatives for LIBs in recent years, particularly in the market of large-scale grid energy storage [7–9]. However, an increased equivalent weight of sodium element and a more positive redox potential for Na^+/Na couple may unavoidably lower the theoretical energy density of SIBs [10–13]. More seriously, the inherent larger ionic size of Na^+ compared with Li^+ (1.02 vs 0.76 Å), further triggers the kinetic challenges involving the sluggish sodium ion diffusion, and the structural instability of the host concerning the large volume changes during the

* Corresponding author.
** Corresponding author.
E-mail addresses: tsham@uwo.ca (T.-K. Sham), xsun9@uwo.ca (X. Sun).

https://doi.org/10.1016/j.nanoen.2019.104177
Received 15 August 2019; Received in revised form 1 October 2019; Accepted 6 October 2019
Available online 9 October 2019

sodiation/desodiation processes. Additionally, the complex sodium chemistry regarding the interactions between cations and host structure as well as subsequent SEI (solid electrolyte interphase) formation/evolution also deteriorates the electrochemical performances of SIBs [8,14]. It is therefore urgent to develop advanced electrode materials with more accessible sodium storage sites and high physiochemical stabilities to promise the sustainability of high-performance SIBs.

Carbonaceous materials have been considered as important choices of anode materials for SIBs, because, up to now, it is yet problematic to directly apply sodium metal as an anode material for SIBs, due to the safety hazards for its low meting point and the inevitable dendrite formation [5]. Compared with the conventional graphite anode for LIBs with an in-plane long range order and a stacking order, which cannot intercalate sodium ions in the formation of thermodynamically stable graphite intercalation compounds (GICs), disordered carbon materials, possessing larger interlayer distances in the irregular structures comprising curved graphene nanosheets and turbostratic graphitic nanodomains, can effectively accommodate the insertion/extraction processes of sodium ions with a larger ionic size [15–25]. Admittedly, typical hard carbon and related materials can deliver reversible capacities around 300 mAh g^{-1}, but the rate performance and cycle stability for these materials are still poor [26–35].

Accordingly, considering the relatively limited electrochemical performances of native carbon materials, various methods have been developed to achieve modified carbon materials with improved electrochemical performances for SIBs. The well-established nanotechnologies in LIBs have been introduced into sodium systems in the fabrication of carbonaceous materials with expanded interlayer distances for buffering the structural strains during the sodiation/desodiation processes, increasing the contact areas between electrodes and electrolyte for an excellent rate capability, and further shortening the pathway lengths for electron transport and sodium ion diffusion [36,37]. Previous research has demonstrated the use of a templated carbon with an hierarchical porosity as an anode material displaying an excellent rate performance [38]. Maier et al. [39] further synthesized hollow carbon nanospheres by a hydrothermal method with a subsequent annealing process and obtained a reversible capacity of 50 mAh g^{-1} at 10 A g^{-1}, while the similar hollow carbon nanowires [40] and the ultrathin hollow carbon nanospheres [41], can both deliver large reversible capacities with an extended cycle life. Notably, the nanostructure designs, ranging from 1D (one-dimensional) carbon nanofibers [42–46]/microtubes [47], 2D (two-dimensional) graphene [48–50]/carbon nanosheets [51,52], to 3D (three-dimensional) carbon frameworks [53–55] and hard carbon matrix [56], have been successfully exemplified in promoting the electrochemical performances of carbon anode materials for SIBs. For example, Ji et al. [45] derived carbon nanofibers from cellulose nanofibers with an excellent rate performance of 85 mAh g^{-1} at 2 A g^{-1} and a superior cycling stability of 176 mAh g^{-1} at 200 mA g^{-1} over 600 cycles. Additionally, a free-standing and binder-free carbon nanofibers electrode obtained from the pyrolysis of PAN-F127/DMF nanofibers through an electrospinning method could also deliver a reversible capacity of ~140 mAh g^{-1} after 1000 cycles at 0.5 A g^{-1} [44]. Moreover, the porous carbon frameworks synthesized from carbon quantum dots presented a remarkable cycle life over 10000 cycles with a highly reversible capacity of 137 mAh g^{-1} at 5 A g^{-1} [54]. In parallel with these developments, much efforts have been devoted to tailoring carbon materials by heteroatom doping for improved electronic conductivities and extra defective sites for sodium ion storage, such as nitrogen doping [57–63], sulfur doping [51,64–67], fluorine doping [68], hydrogen doping [69], and POx doping [70], while biomass-derived carbon materials demonstrated high sodium storage capabilities for their unique porous structures with high disordered degrees [32,34,71–74]. Particularly, the sulfur-doped disordered carbon prepared from carbonizing the mixture of NTCDA and sulfur, displayed a ultra-high reversible capacity of 271 mAh g^{-1} at 1 A g^{-1} over 1000 cycles [64]. Critically, the basic physiochemical properties (interlayer distance, porosity, heteroatom doping, surface area, etc.) would directly affect the sodium storage capability of carbon anode materials [75,76].

Meanwhile, it should be worthy to note that different reaction mechanisms in various electrolytes also determine the sodium intercalation behaviors and subsequent formation/evolution of SEI. Appealingly, graphite was firstly revisited by Adelhelm and colleagues in a diglyme-based electrolyte with a reversible capacity of 100 mAh g^{-1} over 1000 cycles [77], while Kang et al. further optimized the ether-based electrolytes toward a stable specific capacity of 150 mAh g^{-1} for 2500 cycles [78] and observed the formation of solvated sodium ion species in a thermodynamically favorable sodium intercalation process [79]. Upon the emergence of a novel concept for solvent co-intercalation toward sodium ion storage in graphite [80–88], Yang's group further applied a highly porous carbon with a large surface area in ether-based electrolyte and achieved a large reversible capacity of 509 mAh g^{-1} at 100 mA $g^{-1}$with a desirable stability up to 1000 cycles at 1.0 A g^{-1} [83].

Recently, our group demonstrated that a commercial non-porous carbon black can exhibit a significantly improved reversible capacity and an ultralong cycle stability in an ether-based electrolyte [89]. Such improvement is achieved by taking advantage of sodium insertion into the disordered structure and sodium ion-solvent co-intercalation into the graphitic structure. However, the accessible capacity of this pristine carbon black is still low, especially when compared with some reported carbon anode materials. Therefore, a further rational design and engineering of this carbon black is urgently necessary for more active sodium storage sites in ether-based electrolyte.

Herein, we for the first time developed a facile NH_3 etching method to tailor the porosity/microstructure of a commercial carbon black and then tested these porous carbon blacks in an ether-based electrolyte for SIBs. Through incorporating different sodiation/desodiation avenues, we showed that an optimized microporous structure with a minor heteroatom doping and an obvious pseudocapacitive behavior could enable a highly stable capacity with an ultralong cycle life and a remarkable rate performance.

2. Experimental

2.1. Materials preparation

The commercial N330 carbon black was used as the pristine material. Similar as our previous research [90], NH_3 gas was introduced at 1050 °C to etch the N330 carbon black, yielding the porous carbon blacks with the desired mass losses. Typically, 500 mg of N330 powder in a fused silica boat was pyrolyzed in a fused silica reactor under NH_3 at 1050 °C until the desired mass loss is achieved. Samples with the mass loss of 10 wt%, 35 wt%, and 54 wt%, were referred as CBN10, CBN35, and CBN54, respectively.

Sodium triflate ($NaCF_3SO_3$, 98%, Sigma Aldrich) and molecular sieves (4 Å, Sigma Aldrich) were firstly dried at 150 °C in a vacuum oven for 2 days, while molecular sieves were later employed to remove the residual water in the solvents. Two kinds of electrolytes were carefully prepared in an argon-filled glove box by dissolving 1.0 M sodium triflate ($NaCF_3SO_3$, 98%, Sigma Aldrich) into diethylene glycol dimethyl ether (DEGDME, 98.9%, Sigma-Aldrich) and ethylene carbonate (EC, 99%, BASF)/diethyl carbonate (DEC, 99%, BASF) with 1:1 in volume ratio, respectively.

2.2. Physical characterization

The crystalline structures of carbon materials were studied using X-ray Diffraction (XRD) by a Bruker D8Advance (Cu-Kα source, 40 kV, 40 mA) spectrometer, while Raman scattering spectra were recorded using a HORIBA Scientific LabRAM HR Raman spectrometer system equipped with a 532.4 nm laser. A Folio Micromeritics Tristar II surface

area analyzer was employed to measure the N_2 adsorption/desorption isotherm and pore size distribution. Morphologies were observed using a Hitachi S-4800 field emission scanning electron microscope (FE-SEM) operated at 5 keV and a high-resolution transmission electron microscopy (HRTEM) (JEOL 2010 FEG). Synchrotron C K-edge X-ray absorption spectroscopy (XAS) measurements were conducted in Beamline 6.3.1.2 and 8.0.1.4 of Advanced Light Source in Lawrence Berkeley National Laboratory. The C 1s and N 1s X-ray photoemission spectroscopies (XPS) measurements were performed at the high resolution Spherical Grating Monochromator (SGM) beamline in Canadian Light Source (CLS). The high resolution C 1s and N 1s XPS were collected with an excitation energy of 700 eV and a pass energy of 20 eV.

2.3. Electrochemical measurement

Electrodes were prepared by casting the slurry, consisting of 80 wt% active material, 10 wt% acetylene blacks as the conductive agent, and 10 wt% poly(vinylidene difluoride) (PVDF) binder in a suitable amount of N-methyl pyrrolidinone (NMP), onto copper foil. The casted foil was then vacuum dried at 80 °C for 12 h to remove residual water and excess NMP. Then the electrode was punched to ½ inch pellets which were further pressed and found to have a carbon loading mass of ~0.8 mg cm^{-2}. Half-cell configuration 2032-type coin cells were fabricated in an Argon-filled glove box where sodium foil was used as an anode along with a N330 carbon electrode and a polypropylene membrane (Celgard 2400) as cathode and separator, respectively. Finally, the electrochemical properties were evaluated by the cyclic voltammetry (CV) at 0.1 mV s^{-1} and electrochemical impedance spectra (EIS) at an alternating current (AC) voltage of 5 mV amplitude in the 100 kHz to 0.01 Hz frequency range using a Biologic VMP3 electrochemical station. The galvanotactic charge/discharge performances were examined between 0.001 and 2.5 V (vs Na/Na^+) at different current densities under room temperature using an Arbin BT-2000 Battery Tester.

3. Results and discussion

XRD was employed to understand the different microstructures of NH_3-etched porous carbon blacks, as shown in Fig. 1(a). In all patterns, the obviously observed peaks at ~24° and ~42° could be indexed to (002) and (100) diffraction modes, related to the stacking order degree of graphitic carbon structure and the emergence of ordered hexagonal structure, respectively [41,91]. The (002) peak position would slightly move to a low angle, indicating the increased crystal parameters, while its intensity firstly increases and then decreases along with NH_3 etching process. Based on the classic Bragg equation and Scherrer equation [53,91,92], the interlayer distance (d_{002}), the in-lane coherence length (L_c), and the out-of-lane coherence length (L_a) for graphitic domains are calculated as listed in Table S1 (Supporting Information). The apparent decreases of d_{002} as well as L_a and the increase of L_c from CBN10 to CBN54 carbon black clearly reflect the enhancement of short-range ordering and removal of disordered structure. However, during the initial etching process, the L_a value increases while the L_c value decreases from N330 to CBN10 carbon black, which may be attributed to a particular formation mechanism previously investigated [93,94], involving the initial consumption of disordered carbon in the outmost surface part and the following reactions of NH_3 gas with the amorphous carbon from the inner region as well as the graphitic crystallite from the remaining outside edges.

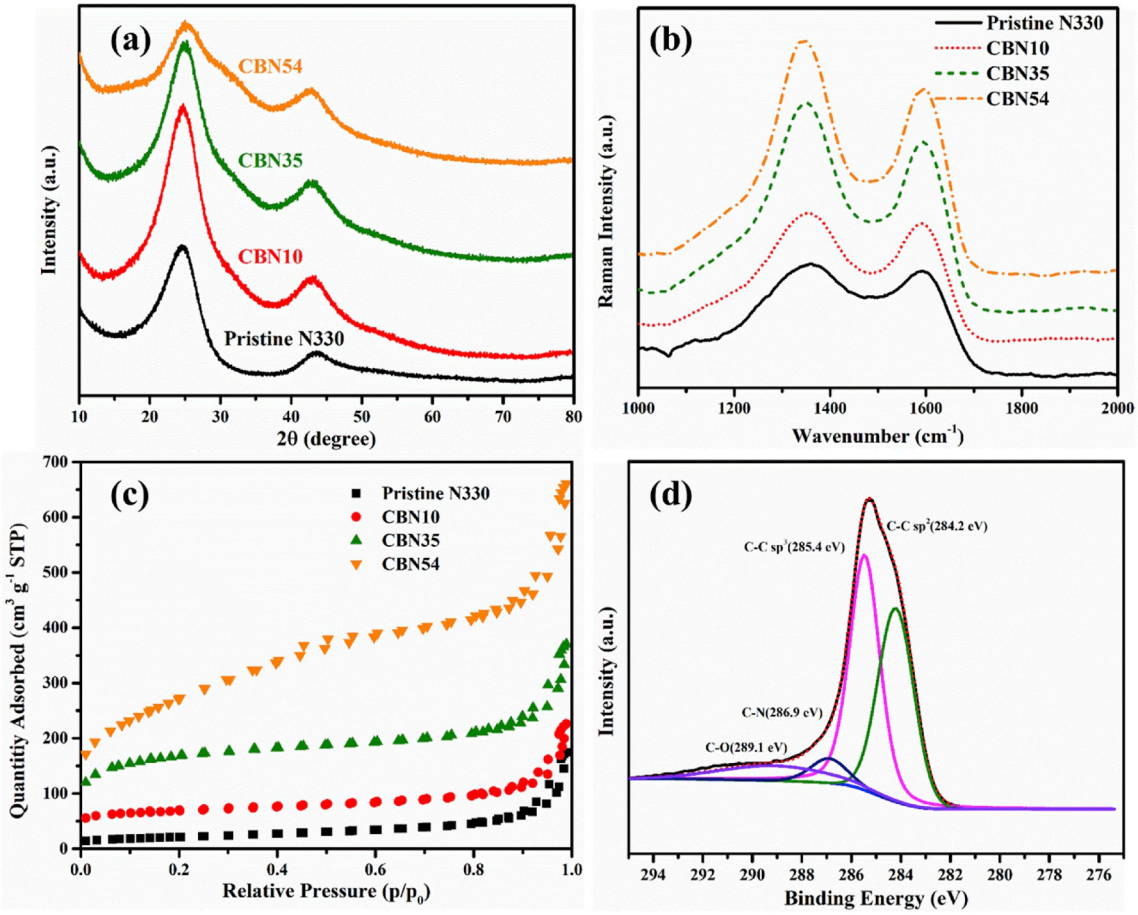

Fig. 1. (a) XRD patterns, (b) Raman spectra, and (c) N_2 adsorption/desorption isotherm spectra for different carbon blacks. (d) Synchrotron-based C 1s XPS for CBN35 carbon black.

Meanwhile, the D band for disordered phase and the G band for graphitic structure in Raman spectra for Fig. 1(b), can be observed around 1343 and 1590 cm^{-1}, respectively. With the proceeding of NH_3 etching process, the corresponding D band would obviously sharpen with a decrease in the width at half maximum (FWHM), which further indicates the gradual diminishment of disordered phase and progressive formation of ordered structure in carbon materials, agreeing well with the results from XRD patterns as well as our previous report [90]. The unusual increase of I_D/I_G upon high-temperature NH_3 etching may be resulted from the curling of stacked graphitic layers and subsequent shrinkage of small graphitic crystals in (100) directions [91,95].

Additionally, Fig. 1(c) presents the nitrogen adsorption-desorption isotherm spectra for different carbon blacks with pore size distributions as compared in Fig. S1. The introduction of reactive NH_3 gas effectively creates the porous structures with the large surface areas, ranging from 78 $m^2 g^{-1}$ for the pristine carbon black to 233, 583, and 783 $m^2 g^{-1}$ for CBN10, CBN35, and CBN54 carbon materials, respectively. Among all samples, the CBN35 carbon black shows a highest specific surface area for microspores. This type of architecture has been shown as the host with most active sites in Fe/N/C catalysts for oxygen reduction reaction at the cathode of proton exchange membrane (PEM) fuel cells [93,94]. Comparing to the previous results from the conventional X-ray photoelectron spectroscopies [90], it can be concluded that N atoms have been successfully doped into the etched porous carbon blacks but with quite limited contents. It is worth noting that the CBN35 carbon black has displayed a highest N doping level of 1.4 wt%, while the CBN10 and CBN54 carbon black have presented a relatively low N doping ratio of 1.0 wt%, as listed in Table S1.

Furthermore, CBN35 carbon black was further characterized by synchrotron-based C 1s XPS and the corresponding single broad peak could be deconvoluted into 4 separate peaks as shown in Fig. 1(d). Two broad peaks centered at 284.2 and 285.4 eV correspond to sp^2 and sp^3 hybridized carbon structures [96–98], respectively, while the comparatively weak peak at 286.9 eV is attributed to C-N bonds (N-sp^3 C configurations, sp^3-hybridized carbon atoms) [99–102]. The appearance of C-O peak for –O-C=O- group at 289.1 eV [101–104] may be originated from immediate contact between etched carbon and air after the pyrolysis, which conforms to our previous conventional XPS results [90]. At the same time, the high-resolution N 1s XPS in Fig. S2 was further employed to identify the composition and configuration of nitrogen species in CBN35 carbon black. Specifically, this broad peak can be accordingly deconvoluted into three dominated peaks locating at 397.5, 399.9, and 402.8 eV, which correspond to the graphitic nitrogen, pyrrolic nitrogen, and pyridinic nitrogen with different atomic ratios of 25.2%, 27.8%, and 47.0%, respectively [105–111]. Specifically, the tap density for pristine N330 carbon black was calculated to 0.44 g cm^{-3}, while the as-obtained CBN35 carbon black was estimated to 0.30 g cm^{-3}, which are still far away from the high tap density of commercial graphite.

Overall, all the above experimental results based on the different characterization methods clearly demonstrate the structural evolution of carbon materials from solid spheres to the microporous and mesoporous carbon nanomaterials after high-temperature NH_3 treatment. This advantageous morphology undoubtedly contributes to the improvements of sodium ion diffusion and intercalation capability of this anode material for SIBs.

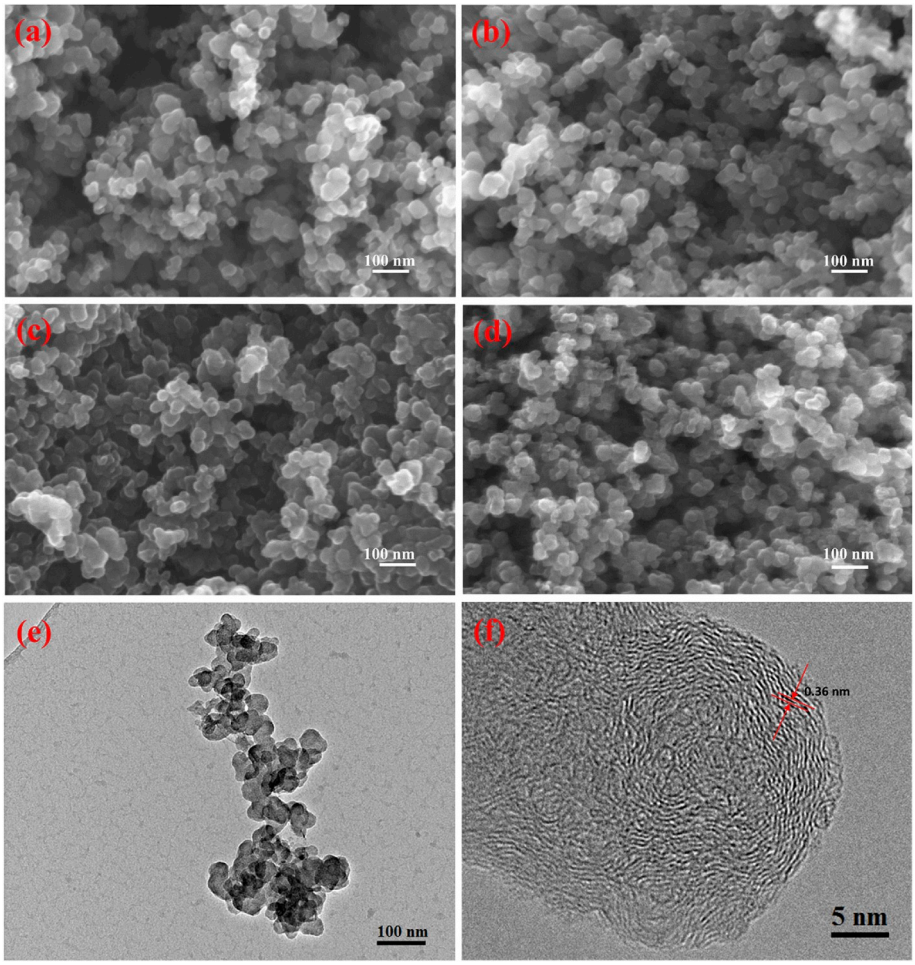

Fig. 2. SEM images of (a) N330, (b) CBN10, (c) CBN35, and (d) CBN54 carbon blacks. (e) TEM image and (f) HRTEM image of CBN35 carbon black.

Fig. 2 depicts the morphologies of different carbon materials. For pristine N330 carbon black as presented in Fig. 2(a), the nanoparticles with different sizes from 20 to 60 nm would severely agglomerate and unevenly distribute. Upon NH_3 etching, several tiny particles (<20 nm) and large particles (>40 nm) disappear and the average particle size become relatively smaller as shown in Fig. 2(b–d) and Fig. S7, which are consistent with the results from our previous particle size distribution analysis [90]. Additionally, TEM and HRTEM images (Fig. 2(e–f) and Fig. S8) highlight an amorphous nature and a few-layer-stacked graphitic structure with an interlayer distance of about 0.36 nm for CBN35 carbon black, which correlates well with data obtained from XRD.

On the basis of the well-understood NH_3 etching mechanism for N330 carbon black [93,94], Fig. 3 further illustrates the carbon porosity formation and microstructure evolution. Normally, the pristine N330 carbon particles consist of a graphitic structure and a disordered phase, but with almost no pore on the surface. At the beginning of the etching process, the outer disordered carbon would firstly be removed under the thermal etching reaction, generating surface pores. With the gradual loss of external disordered carbon, the as-resulted microspores would dimensionally grow deeper and larger, further leading to an increase of specific surface area of micropores and the eventual formation of mesopores. Following the complete consumption of outer disordered carbon, the NH_3 would not only react with the internal disordered part, but also begin to etch remaining graphitic structure near the outer surface. Eventually, the reduction of the outmost graphitic crystallite layer would inevitably result in a decreased particle size.

Based on a synergistic mechanism utilizing both disordered and graphitic structures for sodium storage, it's also critical to study the effects of various porosities on the electrochemical performances. Surprisingly, the etched porous carbon blacks show strikingly different sodium ion storage capabilities at various current densities as compared in Fig. 4. CBN35 carbon black exhibits an initial charge capacity of 352 mAh g^{-1} with a coulombic efficiency of 72.19% at a current density of 50 mA g^{-1}. As shown in Fig. 4(a), the subsequent discharging and charging curves scarcely move while the most sodium intercalation/extraction processes efficiently occur below a voltage of 1.5 V, which is very desirable for coupling with the existing cathode materials in full SIBs. Following 100 cycles of charging/discharging at 50 mA g^{-1}, CBN35 still maintains a highly reversible capacity of 336 mAh g^{-1} with a 95.45% capacity retention as presented in Fig. 4(b). Conversely, the pristine N330 displays an initial reversible of about 234 mAh g^{-1} with an 84.12% capacity retention, while CBN 10 carbon black shows a noticeable capacity decay with a low reversible capacity of about 148 mA mAh g^{-1} and a 76.68% capacity retention in Fig. S3. Additionally, the electrochemical properties of as-obtained porous carbon materials were further studied using an extended cycling galvanostatic charging/discharging at elevated current densities. Comparatively, CBN35 is capable of achieving an initial reversible capacity of about 303 mAh g^{-1} with a coulombic efficiency of 70.79% at 100 mA g^{-1}, while N330 and CBN10 only deliver initial reversible capacities of 213 and 180 mAh g^{-1}, respectively. Different from the rapid capacity degradation for CBN10 with a 58.89% capacity retention, CBN35 carbon retains a stable capacity of about 275 mAh g^{-1} with a 90.76% capacity retention, while N330 carbon has a capacity retention of 77.36% after 200 cycles at 100 mA g^{-1}, as depicted in Fig. 4(c). Upon increasing the current density to 200 mA g^{-1}, CBN35 still delivers a high reversible capacity of 286 mAh g^{-1} with a 69.59% coulombic efficiency in the first cycle. After 400 cycles, an exceptional reversible capacity of 229 mAh g^{-1} with an 80.07% capacity retention is obtained in Fig. 4(d), which is much higher than that of other carbon blacks tested herein. It is worth mentioning that CBN54 carbon black could present a low but stable reversible capacity of about 85 mAh g^{-1} at 50 mA g^{-1} in Fig. S4 without an obvious voltage plateau as well as a capacity loss when increasing the current density, implying its limited active sites for the efficient sodium ion storage, a highly porous carbon structure for the fast sodium ion diffusion after excessive NH_3 etching treatment, and the capacitive behaviors. Specifically, the columbic efficiency used to be a critical parameter to evaluate the electrochemical performance and determine the commercializing feasibility for anode materials. In this case, these crucial values have been systematically compared in Tables S3–S4, while Fig. S10 is employed to observe the changes of columbic efficiencies for various carbon anode materials at a current density of 50 mA g^{-1}. It is obvious to find the as-synthesized CBN35 carbon black would deliver a highest initial columbic efficiency among different samples, further hinting at its superior electrochemical performance after the optimization of microstructure and porosity through NH_3 thermal etching. Additionally, this value would rapidly approach almost 100% in the first 5 cycles and settle at a high level, further indicating its outstanding electrochemical reversibility and durability. Compared with a low reversible capacity and a poor cycle stability obtained for CBN10, the outstanding electrochemical performance of CBN35 carbon is not only resulted from the desirable creation of a highest microporosity with a suitable surface area and more active sodium ion storage sites, but also due to the appropriate structural evolution of graphitic and disordered phases in the noticeable heteroatom-doped carbon

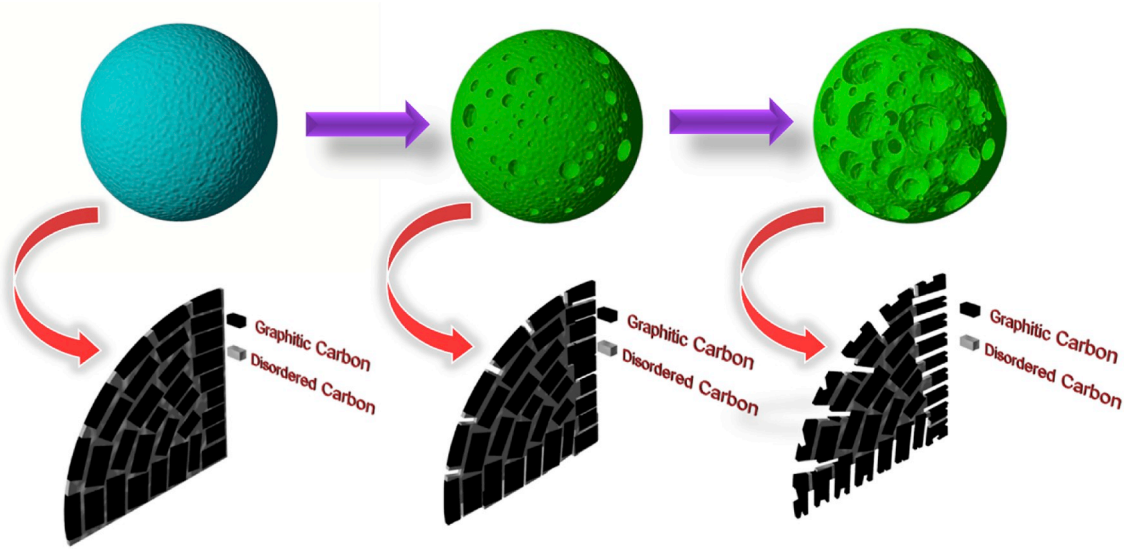

Fig. 3. Schematic diagram of carbon porosity formation and microstructure evolution during the NH_3 etching process.

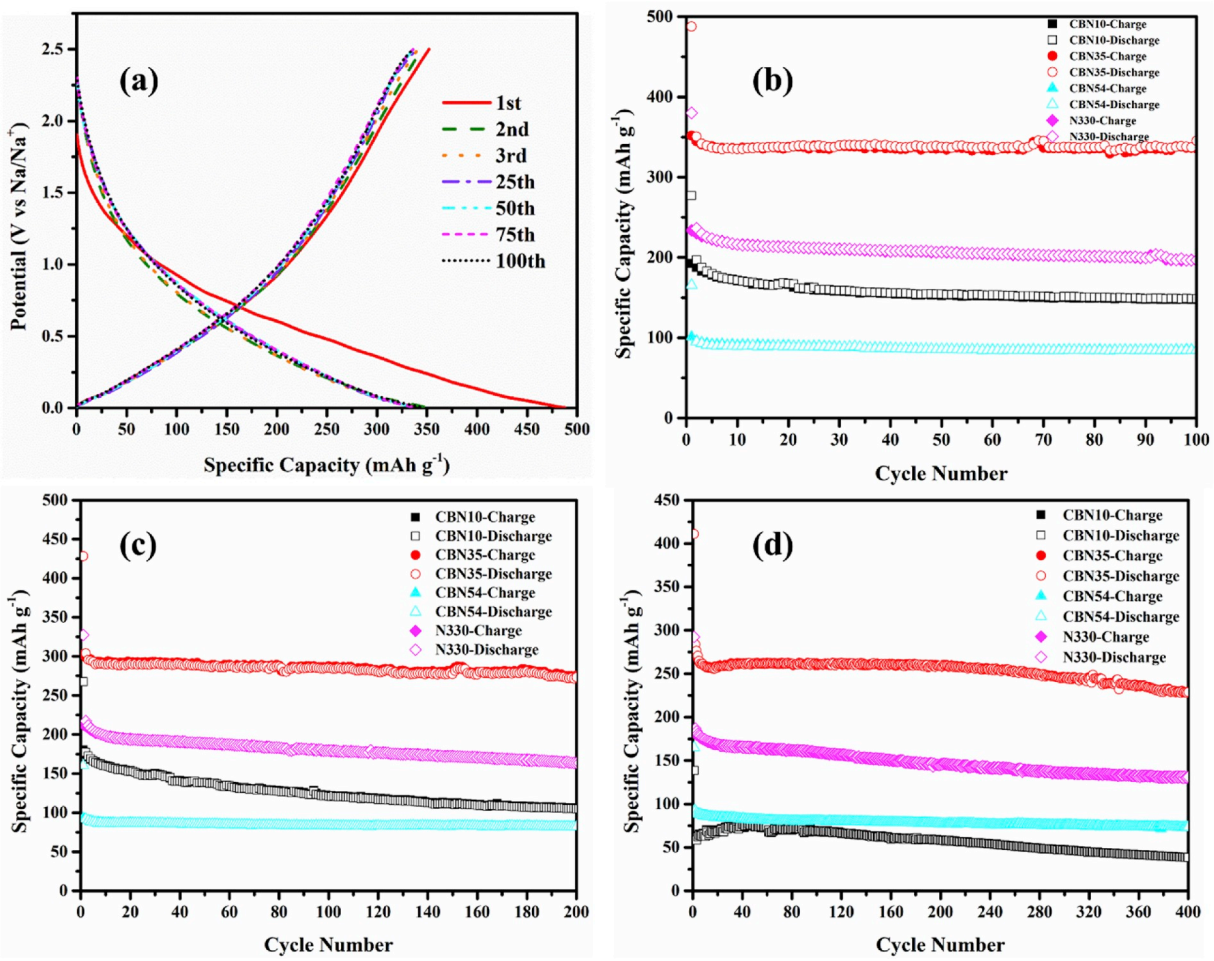

Fig. 4. (a) Discharge-charge profiles for CBN35 carbon black at a current density of 50 mA g^{-1}. Cycle performances of different carbon blacks at current densities of (b) 50, (c) 100, and (d) 200 mA g^{-1}, respectively.

materials for enhancing the solvent co-intercalation behavior in ether-based electrolyte.

The enhanced electrochemical performance and long cycle life seen for CBN35 were also verified in the rate and cycle tests, as displayed in Fig. 5. CBN35 can deliver highly reversible capacities of 339, 306, 298, 280, 259, 237, and 211 mAh g^{-1} at 50, 100, 200, 400, 800, 1600, and 3200 mA g^{-1}, respectively. At the same time, it could still maintain the stable capacities of 184, 164, 149, 136, 126, 115 and 107 mAh g^{-1} at 4800, 6400, 8000, 9600, 11200, 12800, and 14400 mA g^{-1}, respectively. Even when cycled at 16000 mA g^{-1}, a very large capacity of 101 mAh g^{-1} is found in Fig. 5(a–b), demonstrating the electrochemical adaptability of this hierarchal porous structure to extremely high current densities through abundant ion diffusion channels and particular sodium storage mechanisms. After decreasing the current density to 50 mA g^{-1}, the capacity could restore to 337 mAh g^{-1} with a superior electrochemical reversibility. Furthermore, the cycling stability of CBN35 was further evaluated at an ultrahigh current density of 1600 mA g^{-1}. Regardless of a low initial coulombic efficiency of 77.38% and a fast capacity degradation in first 100 cycles for the gradual formation/evolution of SEI, the CBN35 carbon black could deliver an outstanding reversible capacity of 103 mAh g^{-1} over 3200 cycles with a negligible 0.0162% capacity loss per cycle in Fig. 5(c), which is much better than electrochemical properties of carbon-based materials as summarized in Table S5 from most recent reports [32,47,65,69–71,74,91,112–119]. Importantly, the unique microporous structure allows for the facile access to sodium ion storage sites, thereby enabling the rapid reversible sodiation and desodiation processes. Furthermore, the porous nature of this material further facilitates a hybrid swift diffusion of sodium ions and solvated sodium ion species into the disordered and graphitic structures, respectively. Even though the minor N doping may facilitate the migration of electrons and promote the rate capability of carbon materials, the desirable microporous structure with a high surface area would dominantly endow the abundant sodium storage sites on the rich defects, favorably promise the fast transports of sodium ions/solvated compounds upon sodiation/desodiation processes, and further better its wetting capability with electrolyte.

In comparison, with the EC/DEC-based electrolyte, the CBN35 carbon black only exhibits an initial reversible capacity of 127 mAh g^{-1} at 50 mA g^{-1} with a 79.53% capacity retention after 100 cycles, as shown in Figs. S5–S6. This is consistent with our previous results from distinct electrochemical properties for N330 carbon in different electrolytes. Moreover, CV measurements at a scan rate of 0.1 mV s^{-1} were also employed to understand the different electrochemical behaviors of CBN35 in different electrolytes. In EC/DEC-based electrolyte, a strong peak around 0.5 V in first catholic process is observed, as illustrated in Fig. 6(a). This is attributed to the apparent decomposition of electrolyte and the uncontrolled formation of the insulating solid electrolyte interphase (SEI) during the sodiation process. Interestingly, only a small and broad peak can be found in Fig. 6(b) for DEGDME-based electrolyte at around 0.5 V during the first catholic reaction, signaling a weak but noticeable SEI formation process. It's widely recognized that a favorable SEI film would effectively inhibit the continuous decomposition of electrolyte at the low potential and further stabilize the layered structure of graphite anode for a long cycle life [120]. This is especially

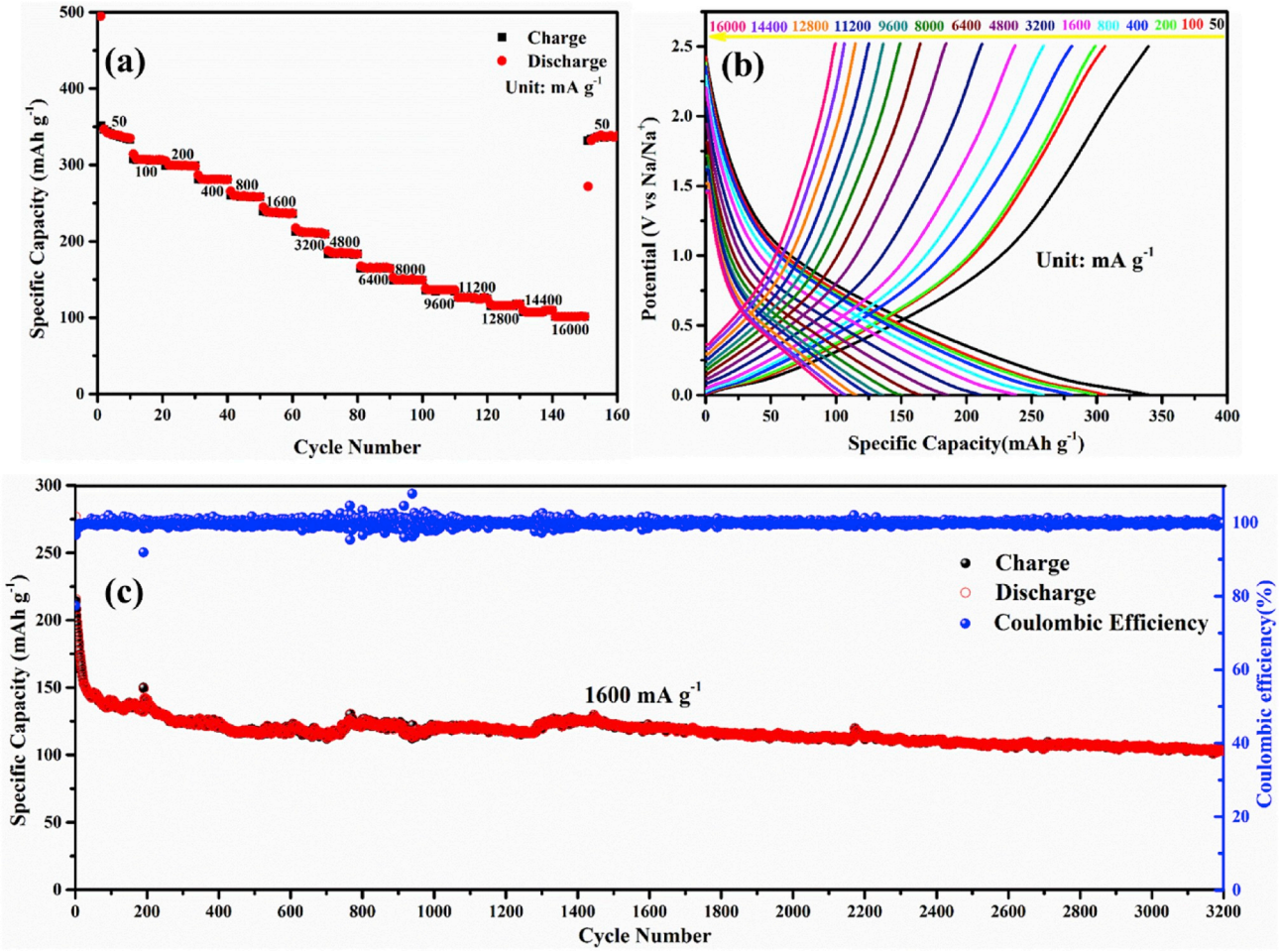

Fig. 5. (a) Rate performance, (b) the corresponding discharging/charging curves at different current densities, (c) cycle performance and coulombic efficiency at a current density of 1600 mA g^{-1} for CBN35 carbon black.

important considering its structural instability towards the solvent co-intercalation for LIBs [121,122]. Nevertheless, the application of ether-based electrolyte in sodium systems with the controlled formation of a thin SEI film seems to be more favorable for enabling a high electrochemical activity and reversibility of porous carbon material [83,88]. Additionally, the EIS results as shown in Fig. 6(c) and Table S2 for discharged CBN35 electrodes using different electrolytes further confirm the underlying role of DEGDME solvent in the performance promotion. In virtue of as-obtained spectra, the SEI impedance between electrode and electrolyte relates to the horizontal axis intercept value in the high frequency region, while the charge transfer resistance results in the semicircle during the medium frequency for discharged electrodes [112]. Compared to the low resistances for discharged electrode in DEGDME-based electrolyte, a slightly increased SEI impedance and a greatly increased charge transfer resistance in EC/DEC-based electrolyte clearly reveal the electrochemical and physiochemical undesirability for uncontrolled formation of a thick SEI layer. This leads to a large amount of electrolyte consumption, which not only lowers the reversible capacity and coulombic efficiency, but also hinders the efficient sodium ion transport for the fast charging/discharging processes. Importantly, the controlling formation of a robust but thin SEI layer would not only suppress the loss of active materials in their side reactions with reactive electrolytes, but also facilitate the migrations of sodium ions and solvated species toward a remarkable rate capability. Furthermore, this negligible and stable SEI would also stabilize the fragile porous structure in carbon anode materials, leading to a superior cycling stability and an ultralong cycle life.

In order to verify the aforementioned phenomenon concerning the controlling formation of SEI thin film for CBN35 carbon black electrode, the surface-sensitive C K-edge X-ray absorption spectroscopies in TEY (Total Electron Yield) mode at different electrochemical states in DEGDME-based electrolyte are investigated in Fig. 6(d). For pristine electrodes, the sharp peaks at 285.4 eV and 292.4 eV are attributed to the carbon 1s core electrons excited to the π*(C-C) and σ*(C-C) orbitals [123], respectively, while the small peak around 288.3 eV may be related to the π*(C=O) transitions [123–126]. Upon discharging to 0.001 V, a new peak appears around 290.1 eV that can be assigned to the σ*(C-O) transitions for the oxygen-containing functional groups from the electrolyte decomposition and SEI formation [126–128]. Simultaneously, the π*(C=O) peak slightly shifts to a high energy region, while peak intensities for both π*(C-C) and σ*(C-C) peaks decrease, further indicating the restrained formation of a SEI film during the discharging process. When charging the electrode back to 2.5 V, the σ*(C-O) peak can still be observed at 290.1 eV, but with a low intensity, indicating a preserved SEI thin film. Therefore, the adoption of an ether-based electrolyte in porous carbon could not only facilitate the fast migrations of sodium ions and solvated sodium ion species across electrolyte/interphase/electrode, but also efficiently enable the controlled SEI formation without sacrificing the reversible capacity and electrolyte amount, leading to the leading to an excellent electrochemical reversibility and an outstanding cycle stability for CBN35.

To reveal the reaction kinetics and sodium storage mechanism for CBN35 carbon black, CV measurements were further performed at various scan rates (0.2–2.0 mV s^{-1}), as shown in Fig. 7(a). Generally, the

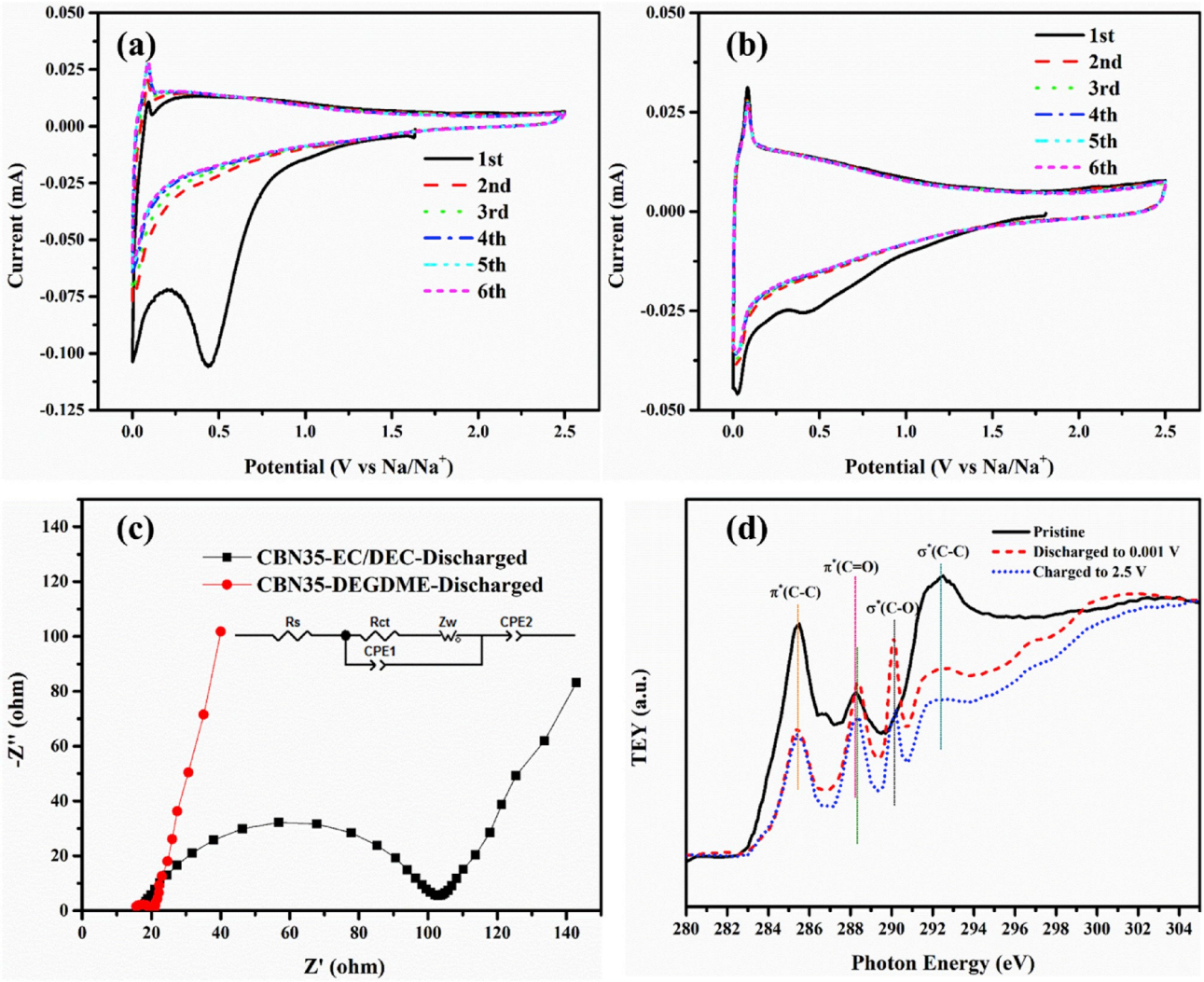

Fig. 6. CV curves of CBN35 carbon black in (a) EC/DEC-based and (b) DEGDME-based electrolytes at 0.1 mV s^{-1}. (c) EIS for discharged electrode in different electrolytes (the inset shows equivalent circuit model). (d) C K-edge X-ray absorption spectroscopies of CBN35 carbon black electrodes at different states when cycling in DEGDME-based electrolyte.

diffusion-controlled process related to the intercalations of sodium ions/solvated compounds into graphitic/amorphous structures and the capacitance-dominated reactions involving the adsorptions of these species on the surface with cavities/nanopores would both contribute to the charge storage in the carbon anode materials for SIBs [67,78,111,129–134], it is necessary to quantitatively identify the diffusive/capacitive contributions in current responses and deeply uncover the charge storage mechanism upon the sodiation/desodiation. Hypothetically, a certain current response has a classical power-law relationship with a corresponding scan rate, which can be described as:

$$i(V) = av^b \tag{1}$$

where i represents an absolute value of current response (mA) at a corresponding voltage of V and v corresponds to a relevant scan rate (mV s^{-1}), while the a and b are adjustable parameters. As the b value at a fixed potential can be facilely derived from a linear fitting of log ($|i(V)|$) versus log(v) profile, the b of 0.5 indicates a Faradaic intercalation reaction in a diffusion-controlled charge storage process, while the b of 1.0 demonstrates a linear relation of current with scan rate in a surface-dominated capacitive charge storage process. Specifically, 30 data points between 0.001 and 2.5 V during the sodiation process have been chosen to calculate the corresponding b values in Fig. 7(b), which would initially approach 1.0 above 0.5 V and gradually decrease to 0.66 V at 0.05 V, hinting a capacitance-dominated process at high potentials and a diffusion-controlled intercalation reaction at low potentials. At the same time, the capacitive charge storage could also be observed by the flat CV curves without electrochemical features at high voltages, while the evolution of CV curves in rectangular shape at increased scan rates further manifests the electrochemical dominance of capacitance-controlled reaction at high rates. Particularly, the sudden drop of b value around 1.0 V in Fig. 7(b) should reflect the increase of intercalation behavior for CBN35 carbon anode during the sodiation process, corresponding with a wide cathodic peak around 1.0 V in CV curve for Fig. 7(c). Additionally, the preservation of redox peaks at various scan rates then confirm the diffusive contribution in a Faradaic intercalation. Regardless of a relatively large anodic peak shift (~0.08 V) from 0.2 to 2.0 mV s^{-1}, the positions of cathodic peak hardly changed at different scan rates, implying a small electrochemical polarization and a desirable reaction kinetics. According to equation (1), the specific capacitive contribution in current response can be further calculated by the following equation:

$$i(V) = k_1 v + k_2 v^{1/2} \tag{2}$$

where $k_1 v$ with the b value of 1.0 and $k_2 v^{1/2}$ with the b value of 0.5 stand for the capacitive and diffusive contributions at a fixed scan rate of v in a certain current response of $i(V)$, respectively. On the basis of a linear

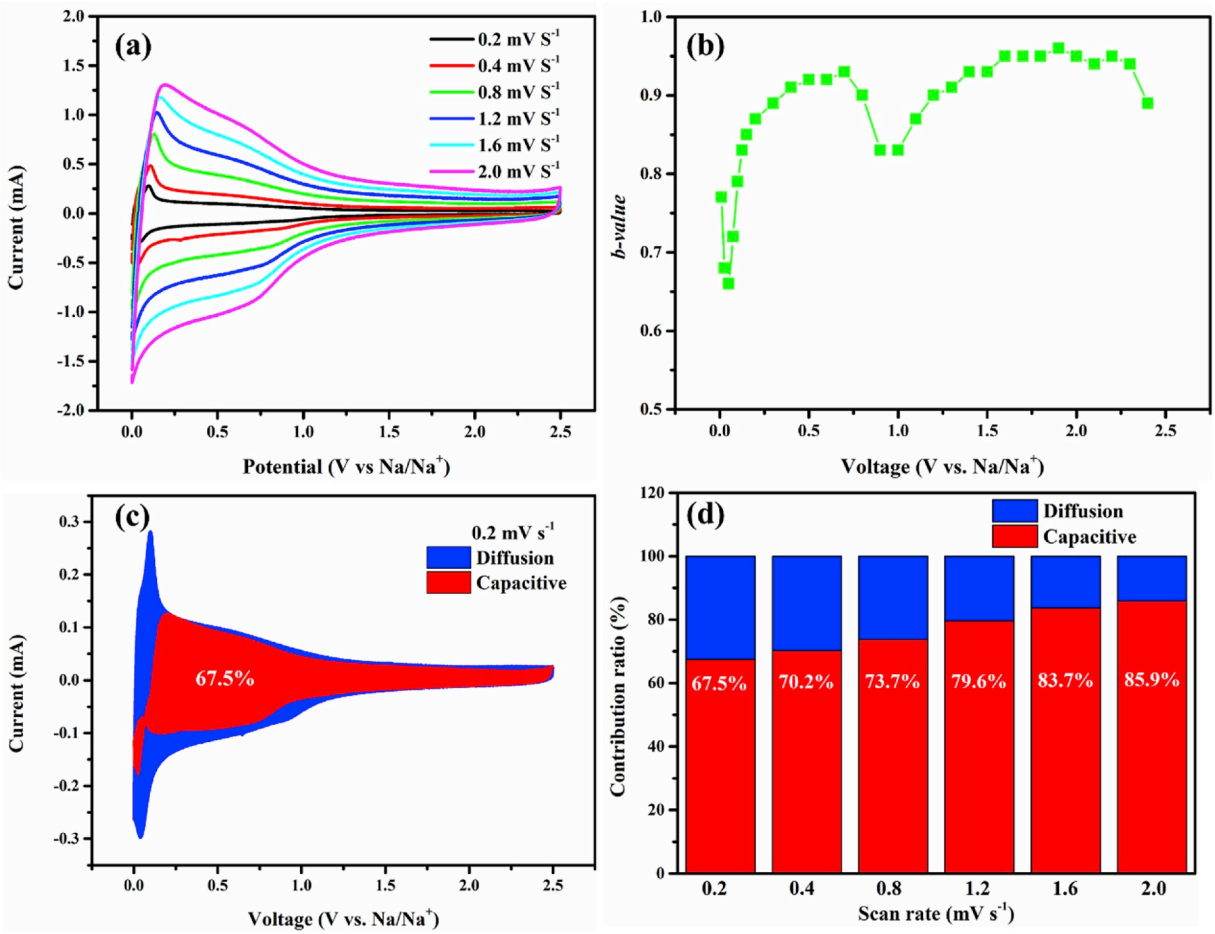

Fig. 7. (a) CV curves of CBN35 carbon black at various scan rates. (b) Calculated *b*-values plotted against the battery potentials for CBN35 carbon black in cathodic (sodiation) process. (c) Capacitive contribution at a scan rate of 0.2 mV s^{-1}. (d) Contribution ratios of capacitive capacity at various scan rates.

fitting for the relationship between $i(V)/v^{1/2}$ and $v^{1/2}$ plot, the specific k_1 values at different voltages can be directly plotted, further yielding the estimated capacitive contributions at various scan rates. As presented in Fig. 7(c), the surface capacitive reaction contributes to a relatively high value of 67.5% in charge storage at 0.2 mV s^{-1}, which may be originated from a desirable microporosity and a hybrid intercalation mechanism for CBN35 carbon black in ether-based electrolyte. When measured at high rates (Figs. S9(b–f) and Fig. 7(d)), the capacitive contribution could reach 70.2%, 73.7%, 79.6%, 83.7%, and 85.9% at scan rates of 0.4, 0.8, 1.2, 1.6, and 2.0 mV s^{-1}, respectively. Importantly, the rapid capacitance-dominated reaction rather than the sluggish sodium ions/solvated species intercalation process would significantly contribute to the sodium storage and ameliorate the rate capability for CBN35 carbon black.

Based on all the data and analysis above, it appears that with assistance of the ether-based electrolyte for the intercalations of both sodium ions and solvated sodium ion species, the intentionally designed porous carbon could deliver an exceptional reversible capacity with a prolonged cycle life. The improved performance results from the desirable formation of microporous structure with more sodium ion storage sites and the controlled formation of a SEI thin film, stabilizing the fragile porous structures and ensuring the rapid sodium ions/solvated sodium ion species transports. At the same time, the obvious pseudocapacitive behaviors on the surface would significantly promote the migrations of sodium ions/solvated compounds and further boost the charge energy storage. In addition to the suitable porosity and microstructure, the surface functionalities can also affect the sodium ion storage capability of carbon-based materials. Such works are ongoing in our group.

4. Conclusions

Porous carbon blacks were initially fabricated using a NH_3 thermal etching method and successfully studied as anode materials for SIBs in an ether-based electrolyte. The as-prepared CBN35 carbon black with a highest microporosity and an appropriate microstructure delivers a large reversible capacity with a superior rate capability and an outstanding cycle stability. The improved sodium storage capability stems from the increased active sites in microporous structure and the novel reaction mechanism, synergistically involving the co-intercalation of solvated sodium ion species into the graphitic structure and the insertion of sodium ions into the disordered structure. Moreover, the excellent rate performance and ultralong cycle stability are also benefitted from the controlled formation/evolution of a robust SEI thin film for a high structural stability, the apparent pseudocapacitive behaviors on the defective surface, and the comparatively fast migrations of sodium ions/solvated species. We believe this work on porous carbon in ether-based electrolyte would enlighten a new strategy to rationally design the nanostructures of carbon materials for high-performance SIBs.

Acknowledgements

This research was supported by the Natural Sciences and Engineering Research Council of Canada, the Canada Research Chair Program (CRC), the Canada Foundation for Innovation, the University of Western Ontario, and the National Natural Science Foundation of China (51672189). Dr. Jian Liu is grateful to the financial support from NSERC

Postdoctoral Fellowships Program. This research used resources of the Advanced Light Source, which is a DOE Office of Science User Facility under contract no. DE-AC02-05CH11231.

Appendix A. Supplementary data

Supplementary data to this article can be found online at https://doi.org/10.1016/j.nanoen.2019.104177.

References

[1] M. Armand, J.-M. Tarascon, Nature 451 (2008) 652–657.
[2] J.M. Tarascon, Phil. Trans. R. Soc. A 368 (2010) 3227–3241.
[3] J.-M. Tarascon, M. Armand, Nature 6861 (2001) 359–367.
[4] B.L. Ellis, L.F. Nazar, Curr. Opin. Solid State Mater. Sci. 16 (2012) 168–177.
[5] M.D. Slater, D. Kim, E. Lee, C.S. Johnson, Adv. Funct. Mater. 23 (2013) 947–958.
[6] V. Palomares, P. Serras, I. Villaluenga, K.B. Hueso, J. Carretero-González, T. Rojo, Energy Environ. Sci. 5 (2012) 5884–5901.
[7] H. Pan, Y.-S. Hu, L. Chen, Energy Environ. Sci. 6 (2013) 2338–2360.
[8] N. Yabuuchi, K. Kubota, M. Dahbi, S. Komaba, Chem. Rev. 114 (2014) 11636–11682.
[9] D. Kundu, E. Talaie, V. Duffort, L.F. Nazar, Angew. Chem. Int. Ed. 54 (2015) 3431–3448.
[10] C. Bommier, D. Leonard, Z. Jian, W.F. Stickle, P.A. Greaney, X. Ji, Adv. Mater. Interfaces 3 (2016) 1600449.
[11] Y. Kim, K.H. Ha, S.M. Oh, K.T. Lee, Chem. Eur J. 20 (2014) 11980–11992.
[12] Y. Fang, L. Xiao, Z. Chen, X. Ai, Y. Cao, H. Yang, Electrochem. Energ. Rev. 1 (2018) 294–323.
[13] T. Wang, D. Su, D. Shanmukaraj, T. Rojo, M. Armand, G. Wang, Electrochem. Energ. Rev. 1 (2018) 200–237.
[14] S.Y. Hong, Y. Kim, Y. Park, A. Choi, N.-S. Choi, K.T. Lee, Energy Environ. Sci. 6 (2013) 2067–2081.
[15] R.C. Asher, J. Inorg. Nucl. Chem. 10 (1959) 238–249.
[16] D.P. DiVincenzo, E.J. Mele, Phys. Rev. B 29 (1984) 1685–1694.
[17] P. Ge, M. Fouletier, Solid State Ion. 28–30 (1988) 1172–1175.
[18] K. Nobuhara, H. Nakayama, M. Nose, S. Nakanishi, H. Iba, J. Power Sources 243 (2013) 585–587.
[19] M.M. Doeff, Y. Ma, S.J. Visco, L.C.D. Jonghe, J. Electrochem. Soc. 140 (1993) L169–L170.
[20] D.A. Stevens, J.R. Dahn, J. Electrochem. Soc. 148 (2001) A803–A811.
[21] C. Bommier, T.W. Surta, M. Dolgos, X. Ji, Nano Lett. 15 (2015) 5888–5892.
[22] Y. Li, Y. Yuan, Y. Bai, Y. Liu, Z. Wang, Limin Li, F. Wu, K. Amine, C. Wu, J. Lu, Adv. Energy Mater. (2018) 1702781.
[23] P. Bai, Y. He, X. Zou, X. Zhao, P. Xiong, Y. Xu, Adv. Energy Mater. (2018) 1703217.
[24] B. Xiao, T. Rojo, X. Li, ChemSusChem 12 (2019) 133–144.
[25] B. Xiao, F.A. Soto, M. Gu, K.S. Han, J. Song, H. Wang, M.H. Engelhard, V. Murugesan, K.T. Mueller, D. Reed, V.L. Sprenkle, P.B. Balbuena, X. Li, Adv. Energy Mater. 8 (2018) 1801441.
[26] D.A. Stevens, J.R. Dahn, J. Electrochem. Soc. 147 (2000) 1271–1273.
[27] P. Thomas, D. Billaud, Electrochim. Acta 47 (2002) 3303–3307.
[28] R. Alcántara, F.J.F. Madrigal, P. Lavela, J.L. Tirado, J.M.J. Mateos, C.G.d. Salazar, R. Stoyanova, E. Zhecheva, Carbon 38 (2001) 1031–1041.
[29] R. Alcántara, J.M. Jiménez Mateos, J.L. Tirado, J. Electrochem. Soc. 149 (2002) A201–A205.
[30] R. Alcántara, J.M. Jiménez-Mateos, P. Lavela, J.L. Tirado, Electrochem. Commun. 3 (2001) 639–642.
[31] R. Alcántara, P. Lavela, G.F. Ortiz, J.L. Tirado, Electrochem. Solid State Lett. 8 (2005) A222–A225.
[32] Y. Li, Y.-S. Hu, X. Qi, X. Rong, H. Li, X. Huang, L. Chen, Energy Storage Mater. 5 (2016) 191–197.
[33] H. Li, F. Shen, W. Luo, J. Dai, X. Han, Y. Chen, Y. Yao, H. Zhu, K. Fu, E. Hitz, L. Hu, ACS Appl. Mater. Interfaces 8 (2016) 2204–2210.
[34] P. Liu, Y. Li, Y.-S. Hu, H. Li, L. Chen, X. Huang, J. Mater. Chem. A 4 (2016) 13046–13052.
[35] P. Bai, Y. He, P. Xiong, X. Zhao, K. Xu, Y. Xu, Carbon 13 (2018) 274–282.
[36] A.S. Aricò, P. Bruce, B. Scrosati, J.-M. Tarascon, W.v. Schalkwijk, Nat. Mater. (2005) 366–377.
[37] P.G. Bruce, B. Scrosati, J.M. Tarascon, Angew Chem. Int. Ed. Engl. 47 (2008) 2930–2946.
[38] S. Wenzel, T. Hara, J. Janek, P. Adelhelm, Energy Environ. Sci. 4 (2011) 3342–3345.
[39] K. Tang, L. Fu, R.J. White, L. Yu, M.-M. Titirici, M. Antonietti, J. Maier, Adv. Energy. Mater. 2 (2012) 873–877.
[40] Y. Cao, L. Xiao, M.L. Sushko, W. Wang, B. Schwenzer, J. Xiao, Z. Nie, L.V. Saraf, Z. Yang, J. Liu, Nano Lett. 12 (2012) 3783–3787.
[41] Y.S. Yun, S.Y. Cho, H. Kim, H.-J. Jin, K. Kang, ChemElectroChem 2 (2015) 359–365.
[42] T. Chen, Y. Liu, L. Pan, T. Lu, Y. Yao, Z. Sun, D.H.C. Chu, Q. Chen, J. Mater. Chem. A 2 (2014) 4117–4121.
[43] J. Jin, Z.-q. Shi, C.-y. Wang, Electrochim. Acta 141 (2014) 302–310.
[44] W. Li, L. Zeng, Z. Yang, L. Gu, J. Wang, X. Liu, J. Cheng, Y. Yu, Nanoscale 6 (2014) 693–698.
[45] W. Luo, J. Schardt, C. Bommier, B. Wang, J. Razink, J. Simonsen, X. Ji, J. Mater. Chem. A 1 (2013) 10662–10666.
[46] P.-Y. Zhao, J. Zhang, Q. Li, C.-Y. Wang, J. Power Sources 334 (2016) 170–178.
[47] Y. Li, Y.-S. Hu, M.-M. Titirici, L. Chen, X. Huang, Adv. Energy Mater. (2016) 1600659.
[48] Y.-X. Wang, S.-L. Chou, H.-K. Liu, S.-X. Dou, Carbon 57 (2013) 202–208.
[49] X.-F. Luo, S.-Y. Wang, C.-M. Tseng, S.-W. Lee, W.-H. Chiang, J.-K. Chang, J. Mater. Chem. A 4 (2016) 7624–7631.
[50] Y. Wang, C. Wang, Y. Wang, H. Liu, Z. Huang, ACS Appl. Mater. Interfaces 8 (2016) 18860–18866.
[51] J. Yang, X. Zhou, D. Wu, X. Zhao, Z. Zhou, Adv. Mater. 29 (2017).
[52] S.Y. Cho, M. Kang, J. Choi, M.E. Lee, H.J. Yoon, H.J. Kim, C. Leal, S. Lee, H.-J. Jin, Y.S. Yun, Small 14 (2018) 1703043.
[53] J. Ding, Huanlei Wang, Z. Li, A. Kohandehghan, K. Cui, Z. Xu, B. Zahiri, X. Tan, E. M. Lotfabad, B.C. Olsen, D. Mitlin, ACS Nano 7 (2013) 11004–11015.
[54] H. Hou, C.E. Banks, M. Jing, Y. Zhang, X. Ji, Adv. Mater. 27 (2015) 7861–7866.
[55] M. Wang, Z. Yang, W. Li, L. Gu, Y. Yu, Small 12 (2016) 2529.
[56] Z. Yuan, L. Si, X. Zhu, J. Mater. Chem. A 3 (2015) 23403–23411.
[57] L. Fu, K. Tang, K. Song, P.A. van Aken, Y. Yu, J. Maier, Nanoscale 6 (2014) 1384–1389.
[58] D. Li, L. Zhang, H. Chen, L.-x. Ding, S. Wang, H. Wang, Chem. Commun. 51 (2015) 16045–16048.
[59] J. Xu, M. Wang, N.P. Wickramaratne, M. Jaroniec, S. Dou, L. Dai, Adv. Mater. 27 (2015) 2042–2048.
[60] F. Yang, Z. Zhang, K. Du, X. Zhao, W. Chen, Y. Lai, J. Li, Carbon 91 (2015) 88–95.
[61] K. Zhang, X. Li, J. Liang, Y. Zhu, L. Hu, Q. Cheng, C. Guo, N. Lin, Y. Qian, Electrochim. Acta 155 (2015) 174–182.
[62] H. Liu, M. Jia, B. Cao, R. Chen, X. Lv, R. Tang, F. Wu, B. Xu, J. Power Sources 319 (2016) 195–201.
[63] D. Yan, C. Yu, X. Zhang, W. Qin, T. Lu, B. Hu, H. Li, L. Pan, Electrochem. Acta 191 (2016) 385–391.
[64] W. Li, M. Zhou, H. Li, K. Wang, S. Cheng, K. Jiang, Energy Environ. Sci. 8 (2015) 2916–2921.
[65] S. Zhang, F. Yao, L. Yang, F. Zhang, S. Xu, Carbon 93 (2015) 143–150.
[66] X. Wang, G. Li, F.M. Hassan, J. Li, X. Fan, R. Batmaz, X. Xiao, Z. Chen, Nano Energy 15 (2015) 746–754.
[67] J. Qian, F. Wu, Y. Ye, M. Zhang, Y. Huang, Y. Xing, W. Qu, Li Li, R. Chen, Adv. Energy Mater. (2018) 1703159.
[68] P. Wang, B. Qiao, Y. Du, Y. Li, X. Zhou, Z. Dai, J. Bao, J. Phys. Chem. C 119 (2015) 21336–21344.
[69] D. Yoon, D.H. Kim, K.Y. Chung, W. Chang, S.M. Kim, J. Kim, Carbon 98 (2016) 213–220.
[70] Z. Li, L. Ma, T.W. Surta, C. Bommier, Z. Jian, Z. Xing, W.F. Stickle, M. Dolgos, K. Amine, J. Lu, T. Wu, X. Ji, ACS Energy Lett 1 (2016) 395–401.
[71] W. Lv, J. Zhao, F. Wen, J. Xiang, L. Li, L. Wang, Z. Liu, Y. Tian, J. Mater. Chem. A 3 (2015) 13786–13793.
[72] K.-l. Hong, L. Qie, R. Zeng, Z.-q. Yi, W. Zhang, D. Wang, W. Yin, C. Wu, Q.-j. Fan, W.-x. Zhang, Y.-h. Huang, J. Mater. Chem. A 2 (2014) 12733–12738.
[73] Y. Li, S. Xu, X. Wu, J. Yu, Y. Wang, Y.-S. Hu, H. Li, L. Chen, X. Huang, J. Mater. Chem. A 3 (2014) 71–77.
[74] R.R. Gaddam, D. Yang, R. Narayan, K. Raju, N.A. Kumar, X.S. Zhao, Nano Energy 26 (2016) 346–352.
[75] C. Bommier, X. Ji, Isr. J. Chem. 55 (2015) 486–507.
[76] M.-S. Balogun, Y. Luo, W. Qiu, P. Liu, Y. Tong, Carbon 98 (2016) 162–178.
[77] B. Jache, P. Adelhelm, Angew. Chem. Int. Ed. 53 (2014) 10169–10173.
[78] H. Kim, J. Hong, Y.-U. Park, J. Kim, I. Hwang, K. Kang, Adv. Funct. Mater. 25 (2014) 534–541.
[79] H. Kim, J. Hong, G. Yoon, H. Kim, K.-Y. Park, M.-S. Park, W.-S. Yoon, K. Kang, Energy Environ. Sci. 8 (2015) 2963–2969.
[80] S.C. Jung, Y.-J. Kang, Y.-K. Han, Nano Energy 34 (2017) 456–462.
[81] Y.-E. Zhu, L. Yang, X. Zhou, F. Li, J. Wei, Z. Zhou, J. Mater. Chem. A 5 (2017) 9528–9532.
[82] L. Seidl, N. Bucher, E. Chu, S. Hartung, S. Martens, O. Schneider, U. Stimming, Energy Environ. Sci. 10 (2017) 1631–1642.
[83] J. Zhang, D.-W. Wang, W. Lv, S. Zhang, Q. Liang, D. Zheng, F. Kang, Q.-H. Yan, Energy Environ. Sci. 10 (2017) 370–376.
[84] B. Jache, J.O. Binder, T. Abe, P. Adelhelm, Phys. Chem. Chem. Phys. 18 (2016) 14299–14316.
[85] Z. Guan, X. Shen, R. Yu, Z. Wang, L. Chen, Electrochim. Acta 222 (2016) 1365–1370.
[86] I. Hasa, X. Dou, D. Buchholz, Y. Shao-Horn, J. Hassoun, S. Passerini, B. Scrosati, J. Power Sources 310 (2016) 26–31.
[87] Z. Zhu, F. Cheng, Z. Hu, Z. Niu, J. Chen, J. Power Sources 293 (2015) 626–634.
[88] M. Goktas, C. Bolli, E.J. Berg, P. Novák, Kilian Pollok, F. Langenhorst, M. v. Roeder, O. Lenchuk, D. Mollenhauer, P. Adelhelm, Adv. Energy Mater. (2018) 1702724.
[89] W. Xiao, Q. Sun, J. Liu, B. Xiao, P.-A. Glans, J. Li, R. Li, J. Guo, W. Yang, T.-K. Sham, X. Sun, Nano Res 10 (2017) 4378–4387.
[90] Y. Li, X. Li, D. Geng, Y. Tang, R. Li, J.-P. Dodelet, M. Lefèvre, X. Sun, Carbon 64 (2013) 170–177.
[91] Y. Li, Y.-S. Hu, H. Li, L. Chen, X. Huang, J. Mater. Chem. A 4 (2015) 96–104.
[92] J. Biscoe, J. Appl. Phys. 13 (1942) 364.
[93] F. Jaouen, J.-P. Dodelet, J. Phys. Chem. C 111 (2007) 5963–5970.
[94] F. Jaouen, A.M. Serventi, M. Lefevre, J.-P. Dodelet, P. Bertrand, J. Phys. Chem. C 111 (2007) 5971–5976.

[95] Y. Li, L. Mu, Y.-S. Hu, H. Li, L. Chen, X. Huang, Energy storage mater 2 (2016) 139–145.
[96] L. Chai, J. Wang, H. Wang, L. Zhang, W. Yu, L. Mai, Nano Energy 17 (2015) 224–232.
[97] R. Haerle, E. Riedo, A. Pasquarello, A. Baldereschi, Phys. Rev. B 65 (2001).
[98] P. Merel, M. Tabbal, M. Chaker, S. Moisa, J. Margot, Appl. Surf. Sci. 136 (1998) 105–110.
[99] C. Morant, J. Andrey, P. Prieto, D. Mendiola, J.M. Sanz, E. Elizalde, Phys. Status Solidi 203 (2006) 1069–1075.
[100] L.H. Chan, K.H. Hong, D.Q. Xiao, T.C. Lin, S.H. Lai, W.J. Hsieh, H.C. Shih, Phys. Rev. B 70 (2004).
[101] R. Jia, J. Chen, J. Zhao, J. Zheng, C. Song, L. Li, Z. Zhu, J. Mater. Chem. 20 (2010) 10829.
[102] X. Yan, T. Xu, G. Chen, S. Yang, H. Liu, Appl. Surf. Sci. 236 (2004) 328–335.
[103] J. Yan, T. Wei, B. Shao, F. Ma, Z. Fan, M. Zhang, C. Zheng, Y. Shang, W. Qian, F. Wei, Carbon 48 (2010) 1731–1737.
[104] S.-Y. Yang, K.-H. Chang, H.-W. Tien, Y.-F. Lee, S.-M. Li, Y.-S. Wang, J.-Y. Wang, C.-C.M. Ma, C.-C. Hu, J. Mater. Chem. 21 (2011) 2374–2380.
[105] S. Liu, J. Zhou, H. Song, Adv. Energy Mater. 8 (2018) 1800569.
[106] Z. Liu, L. Zhang, L. Sheng, Q. Zhou, T. Wei, J. Feng, Z. Fan, Adv. Energy Mater. 8 (2018).
[107] C. Li, Q. Fu, K. Zhao, Y. Wang, H. Tang, H. Li, H. Jiang, L. Chen, Carbon 139 (2018) 1117–1125.
[108] Y. Guo, W. Liu, R. Wu, L. Sun, Y. Zhang, Y. Cui, S. Liu, H. Wang, B. Shan, ACS Appl. Mater. Interfaces 10 (2018).
[109] X. Xu, H. Zeng, D. Han, K. Qiao, W. Xing, M.J. Rood, Z. Yan, ACS Appl. Mater. Interfaces 10 (2018) 37172–37180.
[110] B. Chang, J. Chen, M. Zhou, X. Zhang, W. Wei, B. Dai, S. Han, Y. Huang, Chem. Eur J. 13 (2018) 3859–3864.
[111] L. Liu, Y. Chen, Y. Xie, P. Tao, Z. Wang, Q. Li, K. Wang, C. Yan, Small 15 (2019) 1804158.
[112] L. Xiao, Y. Cao, W.A. Henderson, M.L. Sushko, Y. Shao, J. Xiao, W. Wang, M. H. Engelhard, Z. Nie, J. Liu, Nano Energy 19 (2016) 279–288.
[113] S. Li, J. Qiu, C. Lai, M. Ling, H. Zhao, S. Zhang, Nano Energy 12 (2015) 224–230.
[114] Y. Bai, Z. Wang, C. Wu, R. Xu, F. Wu, Y. Liu, H. Li, Y. Li, J. Lu, K. Amine, ACS Appl. Mater. Interfaces 7 (2015) 5598–5604.
[115] G. Yang, H. Song, H. Cuiab, C. Wang, J. Mater. Chem. A 3 (2015) 20065–20072.
[116] C. Jo, Y. Park, J. Jeong, K.T. Lee, J. Lee, ACS Appl. Mater. Interfaces 7 (2015) 11748–11754.
[117] S. Licht, A. Douglas, J. Ren, R. Carter, M. Lefler, C.L. Pint, ACS Cent. Sci. 2 (2016) 162–168.
[118] Y. Wen, B. Wang, B. Luo, L. Wang, Eur. J. Inorg. Chem. 2016 (2016) 2051–2055.
[119] X. Deng, K. Xie, L. Li, W. Zhou, J. Sunarso, Z. Shao, Carbon 107 (2016) 67–73.
[120] J. Song, B. Xiao, Y. Lin, K. Xu, X. Li, Adv. Energy Mater. 8 (2018) 1703082.
[121] E. Peled, J. Electrochem. Soc. 126 (1973) 2047–2051.
[122] K. Xu, Chem. Rev. 114 (2014) 11503–11618.
[123] J. Zhou, X. Zhou, R. Li, X. Sun, Z. Ding, J. Cutler, T.-K. Sham, Chem. Phys. Lett. 474 (2009) 320–324.
[124] J. Zhou, X. Zhou, X. Sun, R. Li, M. Murphy, Z. Ding, X. Sun, T.-K. Sham, Chem. Phys. Lett. 437 (2007) 229–232.
[125] B. Bouchet-Fabre, M. Pinault, V. Pichot, P. Launois, M. Mayne-L'Hermite, P. Parent, K. Laffon, D. Durand, C. Reynaud, Diam. Relat. Mater. 14 (2005) 881–886.
[126] S.S. Roy, P. Papakonstantinou, T.I.T. Okpalugo, H. Murphy, J. Appl. Phys. 100 (2006), pp. 053703.
[127] S. Banerjee, T. Hemraj-Benny, M. Balasubramanian, D.A. Fischer, J.A. Misewich, S.S. Wong, Chem. Commun. 0 (2004) 772–773.
[128] A. Kuznetsova, I. Popova, J. John, T. Yates, M.J. Bronikowski, C.B. Huffman, J. Liu, R.E. Smalley, H.H. Hwu, J.G. Chen, J. Am. Chem. Soc. 123 (2001) 10699–10704.
[129] X. Yao, Y. Ke, W. Ren, X. Wang, F. Xiong, W. Yang, M. Qin, Q. Li, L. Mai, Adv. Energy Mater. 9 (2019) 1803260.
[130] H. Yang, R. Xua, Y. Yu, Energy Storage Mater. 12 (2019) 105–112.
[131] M. Huang, B. Xi, Z. Feng, J. Liu, J. Feng, Y. Qian, S. Xiong, J. Mater. Chem. A 6 (2018) 16465–16474.
[132] D. Luo, J. Xu, Q. Guo, L. Fang, X. Zhu, Q. Xia, H. Xia, Adv. Funct. Mater. 28 (2018) 1805371.
[133] X. Hu, X. Sun, S.J. Yoo, B. Evanko, F. Fan, S. Cai, C. Zheng, W. Hu, G.D. Stucky, Nano Energy 56 (2019) 828–839.
[134] W. Chen, C. Chen, X. Xiong, P. Hu, Z. Hao, Y. Huang, Adv. Sci. 4 (2017) 1600500.

Wei Xiao is currently a postdoctoral fellow at Xi'an University of Technology in China. He received his bachelor degree of Metallurgical Engineering in 2010 and master degree of Electrochemical Engineering in 2013 from Central South University (China). Later, he achieved his Ph.D. degree in Materials Science and Engineering from University of Western Ontario (Canada) under the supervision of Prof. Xueliang (Andy) Sun and Prof. Tsun-Kong Sham in 2017. His research interests focus on the development of high-performance anode materials for sodium/potassium-ion batteries. His current research works are also related to synchrotron-based X-ray characterizations on energy materials.

Qian Sun is a MITACS Elevate postdoctoral fellow in Prof. Xueliang (Andy) Sun's Group at the University of Western Ontario (Western Univerisity), Canada. He received his B.S. degree in Chemistry in 2006, M.S. degree in Physical Chemistry in 2009, and Ph.D. degree in Applied Chemistry in 2013 under the supervision of Prof. Dr. Zheng-Wen Fu on the study of Li-/Na-ion batteries and Na-air batteries, all at Fudan University, China. He joined Prof. Sun's group in 2013 and his current research interests focus on Na-air, Na-ion, and room temperature Na–S batteries as well as solid-state Li/Na batteries.

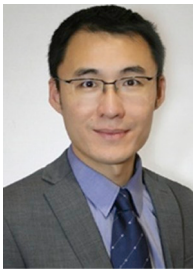

Jian Liu is an Assistant Professor at the University of British Columbia (UBC) Okanagan campus, Canada. Dr. Liu received his Ph.D. in materials science in 2013 from the University of Western Ontario (Canada), and worked as a NSERC Postdoctoral Fellow at Lawrence Berkeley National Laboratory and Pacific Northwest National Laboratory (USA) prior to joining UBC in January 2017. His current research interests focus on advanced nanofabrication techniques, materials design for Li-ion batteries.

Biwei Xiao is a Staff Scientist at Pacific Northwest National Laboratory (PNNL) in the Battery Materials & Systems Group. Prior to that, he was a Ph.D. student at Prof. Xueliang (Andy) Sun's group at The University of Western Ontario, Canada. His research has been associated with the synthesis, modification and mechanism study of electrode materials for sodium-ion batteries and lithium-ion batteries, thin film deposition techniques, synchrotron radiation technique and carbonaceous materials.

Yulong Liu is currently Associate Professor at the Northeast Normal University in China. He received his Bachelor degree from Central South University, China, in 2010, and Master degree in 2013. In 2017, he obtained his Ph.D. degree in Materials Science and Engineering from University of Western Ontario and then became a postdoctoral fellow in Prof. Xueliang (Andy) Sun' Nanomaterials and Energy Group at the University of Western Ontario, Canada. His research interests include nanomaterials for lithium ion batteries, especially $LiFePO_4$ (in collaboration with Phostech Lithium previously and now with Johnson Matthey), and the development of the solid state batteries.

Per-Anders Glans is a research scientist at the Advanced Light Source, Lawrence Berkeley National Laboratory. He obtained his Ph.D. degree in physics from Linköping University in 2001 and has held postdoctoral tenures at Boston University. His research interests include thin films and nanotechnology, material characterization by synchrotron based probing approach.

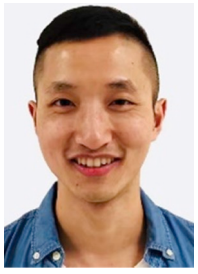

Jun Li is a Marie-Curie fellow at the Ecole polytechnique fédérale de Lausanne (EPFL), Switzerland. Dr. Li received his Ph.D. in Chemistry in 2016 from the University of Western Ontario (Canada), and worked as a Banting Postdoctoral Fellow at University of Toronto prior to joining EPFL in June 2019. His research interests focus on the development of operando/in-situ synchrotron X-ray techniques dedicated to energy materials design for (photo-)electrocatalysis, solar cells and Li-ion batteries.

Ruying Li is a research engineer in Prof. Andy Xueliang Sun's group at the University of Western Ontario, Canada. She received her master degree in materials chemistry in 1999 from the University of Manchester, UK. Then she worked as a research assistant at the University of British Columbia, Canada and L'Institut National de la Recherche Scientifique (INRS), Canada. Her current research interests are focused on advanced materials and characterization for electrochemical energy storage and conversion, including electrocatalysis in fuel cells and electrodes in lithium batteries.

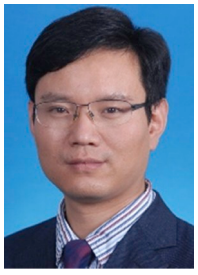

Xifei Li is currently a full professor at Tianjin Normal University and Xi'an University of Technology. Prof. Li's research group is currently working on design, synthesis as well as performance improvement of the anodes and the cathodes with various structures for high performance lithium ion batteries, lithium sulfur batteries, sodium ion batteries, and supercapacitors. He has authored and co-authored over 190 refereed journal articles with more than 7400 citations, two invited book chapters as well as 13 patents.

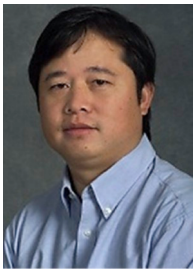

Jinghua Guo is a senior scientist at the Advanced Light Source, Lawrence Berkeley National Laboratory, and adjunct professor in the Department of Chemistry and Biochemistry, University of California, Santa Cruz. He received the Ph.D. in physics at Uppsala University, Sweden, in 1995. He is one of the world's leading experts in the research fields of in-situ/operando soft X-ray spectroscopy. His research interest focuses on the electronic structure, chemical bonding and charge transfer in energy-conversion and energy-storage materials and devices.

Wanli Yang is a staff scientist at the Advanced Light Source division of Lawrence Berkeley National Laboratory. He received his bachelor's degree in physics from Shandong University in China, and his Ph.D. degree in physics from Institute of Physics, Chinese Academy of Sciences. He was a postdoc and then a staff scientist at Stanford University after graduation. His current research interest focuses on soft x-ray spectroscopy of battery materials, including electrode, electrolyte, and interphase materials.

Prof. T.K. Sham is a Distinguished University Professor and a Canada Research Chair in Materials and Synchrotron Radiation at the University of Western Ontario. He obtained his PhD from the University of Western Ontario (1975) with a BSc from the Chinese University of Hong Kong. He joined the Chemistry Department at Brookhaven National Laboratory in 1977 and returned to Western in 1988. He is presently the Director of the Soochow-Western Centre for Synchrotron Radiation, a Fellow of the Royal Society of Canada and an Officer of the Order of Canada. Dr. Sham's expertise are nanomaterial synthesis, surface and interface, X-ray absorption related spectroscopy and microscopy. His recently focus is nanostructure phase transition, assembly of nanocomposites, in situ/in operando studies of energy materials and devices. X-ray excited optical luminescence in the energy and time domain, nanomaterials for drug delivery, and micro-beam analysis of cultural and heritage materials.

Prof. Xueliang (Andy) Sun is a Canada Research Chair in Development of Nanomaterials for Clean Energy, Fellow of the Royal Society of Canada and Canadian Academy of Engineering and Full Professor at the University of Western Ontario, Canada. Dr. Sun received his Ph.D. in materials chemistry in 1999 from the University of Manchester, UK, which he followed up by working as a postdoctoral fellow at the University of British Columbia, Canada and as a Research Associate at L′ Institut National de la Recherche Scientifique (INRS), Canada. His current research interests are focused on advanced materials for electrochemical energy storage and conversion.